



Kinetic interactions between H₂ and CO in catalytic oxidation over PdO

Ran Sui^{a,*}, Wenkai Liang^a, Liang Zhang^b, John Mantzaras^c, Chung K. Law^{a,d,**}

^a Department of Mechanical and Aerospace Engineering, Princeton University, Princeton, NJ 08544, USA

^b Department of Chemical and Biomolecular Engineering, University of Connecticut, Storrs, CT 06269, USA

^c Laboratory for Scientific Computing and Modeling, Paul Scherrer Institute, Villigen PSI, CH-5232, Switzerland

^d Center for Combustion Energy, Tsinghua University, Beijing 100084, China

ARTICLE INFO

Article history:

Received 27 May 2019

Revised 14 June 2019

Accepted 26 September 2019

Keywords:

Catalytic combustion

Syngas

Palladium catalyst

Surface kinetics

H₂–CO kinetic interactions

Coverage-dependent activation energies

ABSTRACT

Kinetic interactions between H₂ and CO over PdO, a widely used catalyst in combustion systems, were studied experimentally and numerically. Global reaction parameters of H₂ and CO oxidation over PdO were extracted from wire microcalorimetry experiments at atmospheric pressure in the temperature range 380–800 K, based on which a full catalytic reaction mechanism was developed. Comparison of ignition temperatures and heat release rates of different H₂/CO blends along with density functional theory (DFT) simulations revealed complex physicochemical coupling of the H₂ and CO catalytic oxidation pathways. The coupling evolves from an inhibiting effect of one fuel component onto the other due to their competition for surface adsorption sites and a direct repelling mechanism between the co-adsorbed H(s) and CO(s), to a promoting effect at sufficiently high temperatures caused by alleviated O(s) surface blocking. Implications of the H₂–CO kinetic coupling to the operation of practical power generation systems are outlined.

© 2019 The Combustion Institute. Published by Elsevier Inc. All rights reserved.

1. Introduction

Combustion of syngas, a gas mixture primarily consisting of hydrogen and carbon monoxide, has drawn much attention in recent years as an environmentally clean fuel that can facilitate reduced emissions in gas turbines of power generation systems [1–4]. Specifically, greenhouse gas emissions can be controlled via pre-combustion CO₂ capture, accomplished by reforming of natural gas or gasification of solid biomasses to syngas, subsequently converting large part of the produced CO to CO₂ in a water–gas-shift reactor (WGS) and finally capturing the formed CO₂ prior to combustion [5,6]. Another method of mitigating CO₂ emissions in gas turbines is the post-combustion capture of CO₂, which is typically accomplished with flue gas recycle (FGR); in this case the addition of high-hydrogen content syngas is very beneficial, as it increases the reactivity of the heavily-diluted reactant stream [7]. Syngas fuels are also suited for the enhancement of combustion stability and emission reduction in automotive internal combustion engines [8] and micro-scale portable power generation systems [9].

Of particular interest for the present investigation are the hybrid catalytic/gaseous combustion methodologies, as they can mitigate flame flashback of the very reactive high-hydrogen content syngas fuels inside the channels of typical honeycomb catalytic reactors [10]. In both pre- and post-combustion CO₂ capture methods, catalytic reactions can be utilized with the catalytically stabilized thermal combustion (CST) concept, in which fractional fuel conversion is achieved heterogeneously in a reactor that is typically coated with a noble metal, while the remaining fuel is subsequently consumed homogeneously in a gaseous combustion zone [11]. Furthermore, CO addition is of special benefit in H₂-fueled catalytic reactors as it moderates the surface superadiabaticity induced by the diffusional imbalance of hydrogen [9,12] thus facilitating reactor design and thermal management [1,13].

Palladium is a widely used noble metal catalyst for methane oxidation [13–16]. Furthermore, because of its superior low-temperature activity in methane oxidation, palladium-based catalysts have been prime choices as front-face catalysts in natural gas fueled turbine combustors as well as microreactors [14,17,18]. Recently, a non-monotonic pressure dependence of the methane catalytic reactivity on PdO was observed [18,19], which is contrary to the monotonically increasing pressure dependence of the methane reactivity on other noble metals (Pt, Rh) [20,21], while a microkinetic model was developed for methane oxidation over PdO that

* Corresponding author.

** Corresponding author at: Department of Mechanical and Aerospace Engineering, Princeton University, Engineering Quadrangle, 40 Olden Street, Princeton, NJ 08544, USA.

E-mail addresses: rsui@princeton.edu (R. Sui), cklaw@princeton.edu (C.K. Law).

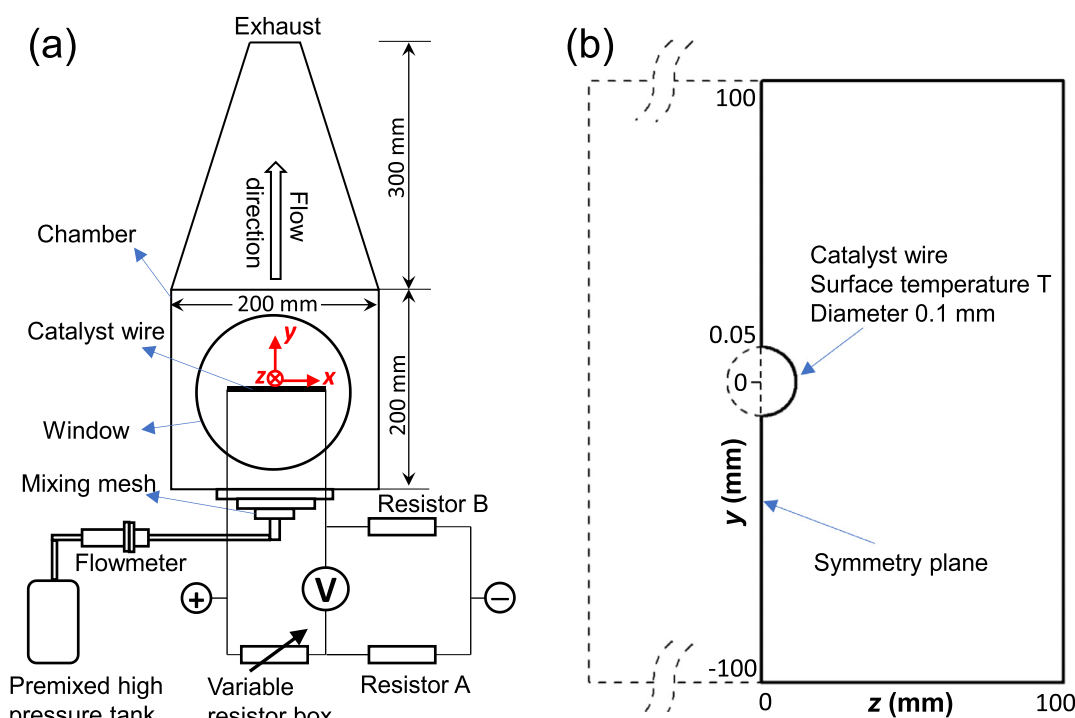


Fig. 1. (a) Schematic of the wire microcalorimetry flow system. The catalyst wire, variable resistor box and two resistors constitute a bridge circuit. (b) Schematic of the 2D computational domain, adapted with permission from [26], copyright (2013) American Chemical Society.

captures the hysteresis in PdO/Pd decomposition and re-oxidation [22].

In view of the practical importance of the catalytic oxidation of syngas over palladium, and given that several surface reaction mechanisms for the oxidation of simple fuels over palladium have been reported [23–27], it is timely to conduct dedicated kinetic studies of syngas mixtures on palladium. Such studies are complicated by the intricate interplay between the two fuel components, H_2 and CO, and the complex temperature and pressure dependent phase change (Pd/PdO_x) of palladium-based catalysts [28,29]. Consequently, the primary objective of the present work is to investigate the heterogeneous kinetics of syngas over palladium-based catalysts and the associated physicochemical interactions between the H_2 and CO fuel components.

This paper is organized as follows. First, the adopted experimental and numerical methodologies are introduced in Sections 2 and 3, respectively. Next, the global and detailed reaction parameters for H_2 oxidation on PdO, extracted from wire microcalorimetry experiments, are reported in Section 4.1. In Section 4.2 the CO-poisoning effects on the PdO catalyst and the determination of separate H_2 and CO reactions over the poisoned catalyst are presented. The combustion of H_2 /CO mixtures and the kinetic coupling between H_2 and CO on PdO surfaces are subsequently discussed in Section 4.3, wherein a detailed syngas reaction mechanism is formulated. The main results are summarized in Section 5.

2. Experimental

The experiments employed the wire microcalorimetry technique that has been detailed previously [26,30] and is briefly described next. The experimental setup is schematically illustrated in Fig. 1(a). A pre-oxidized polycrystalline PdO wire, 100 μ m in diameter and 100 mm in length, is positioned horizontally in the center of a fixed-pressure closed rectangular chamber (with horizontal cross-stream area of 200×200 mm² and height of 200 mm). The gaseous environment is perpetually replenished with a verti-

cal creeping gas flow (10 mm/s). Independence of heat release rate on the inlet velocity is assured at low temperatures and low flow rates, such that the wire can be essentially considered as being immersed in a constant concentration bath. A previous study [31] has shown that the ignition temperature of H_2 /air mixtures is independent of the flow velocity under similar conditions. In addition, with very low flow rates, flow separation, recirculation and upstream-to-downstream convective transport are minimized, and thus uniform properties on the catalyst wire are ensured.

By passing an electric current the wire is heated in an air stream to a temperature T with a power $P_1(T)$. The wire temperature is determined by a relation $R(T)$ between the temperature T and the electric resistance R . The gases are well premixed in a high-pressure tank before entering the chamber, whose entrance is also equipped with a mixing mesh. In addition, the wire temperature is real-time monitored and very stable values are obtained during each test. A reactive mixture with a small amount of fuel is then introduced into the flow and the power is adjusted to $P_2(T)$ in order to maintain the same wire temperature T . Since the diffusive-convective heat loss from the wire to the environment is the same with the wire temperature maintained at T , the difference in the heating powers at T , $\Delta P(T) = P_1 - P_2$, gives the catalytic heat release rate at T . By continuously varying T , a relation $\Delta P(T)$ is determined, which subsequently yields the global catalytic reaction rate as well as the ignition temperature at which the reaction rate abruptly increases above zero. Experiments were carried out at atmospheric pressure and temperatures up to 800 K to avoid PdO decomposition to Pd and catalyst deactivation.

The catalyst wire surface is fully oxidized to PdO using a metallic Pd wire following a standard treatment that allows for a stable surface morphology and reproducible catalytic reactivity [26,27,30]. The surface morphology and phase composition of the catalyst wire before and after the oxidation treatment are determined via Scanning Electron Microscopy (SEM) and Energy-dispersive X-ray spectroscopy (EDX) measurements. Figure 2(a) and (b) provides surface SEM images of the smooth fresh wire and the porous oxidized wire (heated to 900 K), indicating a surface morphology

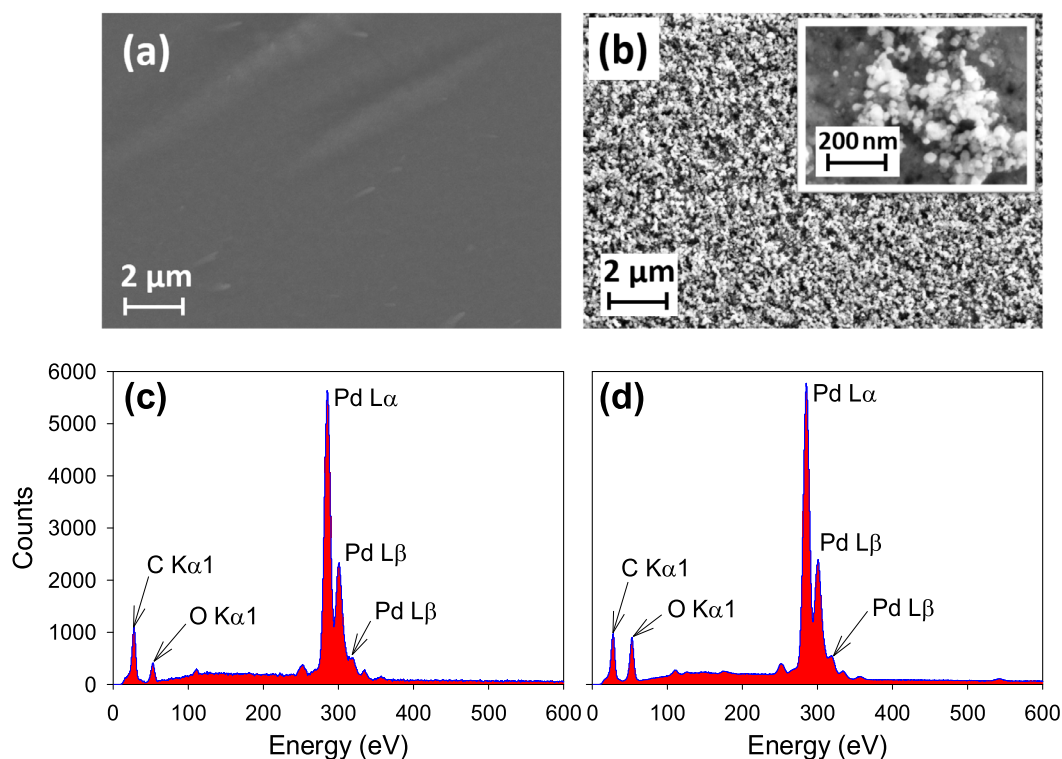


Fig. 2. Surface SEM images of (a) a fresh catalyst wire and (b) an oxidized catalyst wire following the standard procedure at 900 K [26,30]. EDX spectra of the corresponding fresh (c) and oxidized (d) wires. Oxygen weight increased from 8.0% (c) to 17.1% (d).

development from a smooth polycrystalline structure to a porous layer. Previous studies using the same wire samples have shown a $\sim 2\mu\text{m}$ thickness of the PdO layer [26,30]. These observations assure an oxidized catalyst surface, which is consistent with earlier XPS observations [18,26,30]. EDX measurements in Fig. 2(c) and (d) confirm the increased oxidation state of the heated palladium wire.

3. Numerical

In the numerical part, two investigations have been pursued. First, 2D simulations over half the y - z domain (schematic of the computational domain is shown in Fig. 1(b) and details in [32]) with the Fluent code were carried out; the code has been validated against past wire microcalorimetry experiments [26,27,32,33] in simulations with detailed methane catalytic and gas-phase reaction mechanisms. Gravity in the y -direction was included in the simulations. In the present work, a detailed catalytic reaction mechanism was developed based on the H_2/CO subset of a thermodynamically consistent CH_4 mechanism in a recent PdO wire microcalorimetry study [26], with the important reactions for syngas, i.e. adsorption and desorption reactions of H_2 and CO on PdO first amended individually. Subsequently, kinetic interactions between H_2 and CO oxidation were modeled and compared against experimental data and the catalytic reaction mechanism was updated. A detailed gaseous H_2/CO reaction scheme [34] was also included in the simulations. Such simulations ensured the negligible impact of gas-phase reactions, which in turn negated potential falsification of surface kinetics by gaseous kinetics.

The second numerical investigation included density functional theory (DFT) calculations on a (1×3) PdO(101) surface to further unravel the interactions between H_2 and CO adsorption processes. All calculations were performed using the Quantum ESPRESSO package [35] in combination with Atomic Simulation Environment [36] based on plane-wave DFT methods. Exchange and correlation were described by generalized gradient approximation (GGA) us-

ing the Perdew–Burke–Ernzerhof (PBE) functional [37]. Kohn–Sham wave functions were expanded in a plane-wave basis with a kinetic energy cutoff of 450 eV. A vacuum spacing of at least 14 Å was added to all supercell models to avoid interaction between periodic images. All geometries were considered optimized when the maximum force on each atom was less than 0.01 eV/Å. Transition states and the corresponding reaction barriers used the climbing-image nudged elastic band method (CI-NEB) [38,39]. Both plane wave cutoffs and k -point grid density were checked for convergence with respect to chemisorption energies.

4. Results and discussion

4.1. Reaction parameters of H_2 oxidation on PdO

Global reaction parameters of H_2 oxidation over PdO were first extracted from the heat release measurements. To ensure negligible changes in the heat transfer properties of the reactive mixtures and air [40] and to avoid distortion from the moisture accumulated in the PdO porous structure, only up to 1.0% vol. H_2 was doped into air. Self-inhibiting kinetic effect [23] of H_2 on the catalytic ignition over PdO was observed, with measured ignition temperatures 380 K, 385 K and 389 K for H_2 volumetric concentrations 0.25%, 0.5% and 1.0%, respectively. Data were obtained within the kinetically controlled regime at temperatures up to 410 K, above which reactions became fast and fell into the mixed kinetic/transport-controlled regime. As shown in Fig. 3(a), independence of heat release rate on the inlet velocity was assured at temperatures below 410 K and inlet flow velocities ~ 6 –25 mm/s. For the $2\mu\text{m}$ catalyst layer thickness and for the calculated apparent reaction rates herein, the Thiele modulus ϕ was quite small ($\phi < 0.08$ over the temperatures of the present kinetic investigation), indicating that surface reaction instead of internal diffusion is the limiting process. In addition, Fig. 3(b) provides the computed radial profiles of the H_2 mass fraction Y_{H_2} , normalized by the inlet H_2 mass fraction

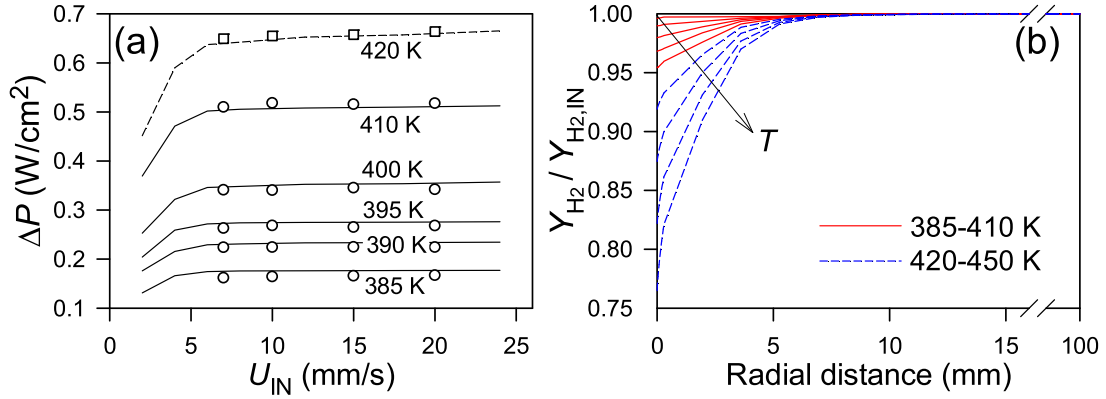


Fig. 3. (a) Measured (symbols) and computed (lines, using the reaction mechanism of Table 1) heat release rates of 0.5% vol. H_2 in air at 385–420 K and 2–24 mm/s inlet velocity. (b) Computed normalized radial profiles of H_2 mass fraction $Y_{H_2}/Y_{H_2,IN}$ at temperature ranges 385–410 K (solid lines) and 420–450 K (dashed lines), inlet velocity 15 mm/s.

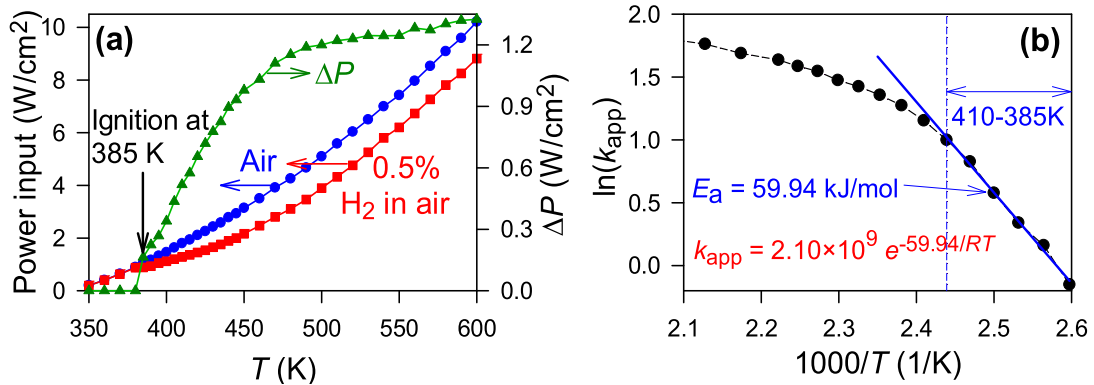


Fig. 4. (a) Electrical power input needed to maintain PdO wire temperatures in air (circles) and reactive mixture (0.5% vol. H_2 in air, squares) flows. The difference yields the catalytic heat release rate ΔP (triangles). (b) Arrhenius plot of (a), experimental data (symbols and dashed line) and linear fit (solid line).

$Y_{H_2,IN}$, near the PdO wire. Below 410 K the near-wall H_2 mass fractions were 95.4–99.6% of the inlet mixture, manifesting a strongly kinetically-controlled regime with negligible external diffusion limitations within the temperature range where the kinetics has been evaluated. The profiles in Fig. 3(b) are largely similar for all azimuthal positions, as gravity does not significantly affect them.

Figure 4 provides the ignition temperatures, the measured heat release rates over the range 385–600 K (with 30 temperature points) and the Arrhenius plot for the case with 0.5% vol. H_2 in air. Considering O_2 is in large excess, the apparent reaction rate of H_2 can be expressed as:

$$\dot{s}_{H_2} = \Delta P / (R_{eff} \Delta H_f) = k_{H_2}^{app} [H_2] \quad (\text{mol/cm}^2/\text{s}) \quad (1)$$

where ΔH_f denotes the enthalpy of combustion of hydrogen (lower heating value). The effective surface area R_{eff} was found to be 3.5 times the area of an ideal cylinder in a recent PdO wire microcalorimetry study via atomic force microscopy (AFM) measurements [26] and attested via a CH_4 oxidation as in [26] after the H_2 measurements. As deduced from Fig. 4(b) for 0.5% vol. H_2 in air over the temperature range 385–410 K, the global rate of H_2 /air over PdO has the following reaction coefficients (averaged for three conditions, 0.25%, 0.5% and 1.0% vol. H_2 in air):

$$k_{H_2}^{app} = (2.45 \pm 0.35) \times 10^9 e^{-(61.74 \pm 1.80) \text{ (kJ/mol)}/RT} \quad (\text{cm/s}) \quad (2)$$

The rate coefficients of H_2 adsorption and desorption in the original reaction mechanism of Table 1 were subsequently amended based on the global step of H_2 oxidation over PdO, as the overall H_2 conversion rate can be expressed as:

$$\dot{s}_{H_2} = k_{H_2}^{app} [H_2] = k_{1f} [H_2] (\Gamma \theta_{Pd(s)})^2 - k_{1b} (\Gamma \theta_{H(s)})^2 \quad (\text{mol/cm}^2/\text{s}) \quad (3)$$

where Γ denotes the surface site density of the catalyst, while $\theta_{Pd(s)}$ and $\theta_{H(s)}$ are the free site fraction and $H(s)$ occupied site fraction, respectively. Considering that the backward reaction after ignition is minute, the forward reaction constant can be obtained via

$$k_{1f} \approx k_{H_2}^{app} / (\Gamma \theta_{Pd(s)})^2 \quad (4)$$

where k_{1f} is implicitly coupled with the free surface site fraction $\theta_{Pd(s)}$. The negligible magnitudes of H_2 desorption after ignition were attested by simulations in a surface perfectly stirred reactor (SPSR) [41] at 385–410 K, which indicated 10 orders of magnitude smaller desorption rates than adsorption rates. This behavior was similar to that reported for H_2 over other noble metals (Pt [42] and Rh [43]). Using the literature value for the sticking coefficient ($\gamma = 1.0$) [26] as an initial guess in the Fluent simulations, k_{1f} was fine-tuned iteratively against the wire microcalorimetric data. The iterative procedure is as follows: For each fixed temperature, $\gamma = 1.0$ is used in the first Fluent simulation, from which a free surface site fraction $\theta_{Pd(s)}$ is obtained. k_{1f} is subsequently updated using Eq. (4), $k_{1f} = k_{H_2}^{app} / (\Gamma \theta_{Pd(s)})^2$, where $k_{H_2}^{app}$ has been determined as in Eq. (2). The pre-exponential and activation energy of R1f are obtained from the Arrhenius plot of k_{1f} , and are used in the next Fluent simulation. $\theta_{Pd(s)}$ is updated again and, followed by a new k_{1f} via Eq. (4). This iterative procedure is repeated until the value of k_{1f} converges. In the Arrhenius expression, $k_{1f} = AT^b \exp(E_a/RT)$, the activation energy was

Table 1
Surface reaction mechanism of H₂ oxidation over PdO^a.

No.	reaction	A	b	E _a
1f	H ₂ + 2Pd(s) → 2H(s)	2.80 × 10 ²⁶	0.00	57.33
1b	2H(s) → 2Pd(s) + H ₂	8.43 × 10 ²²	0.992	142.82
3f	O ₂ + 8Pd(s) → 2O(s)	$e^{-T/540-8.8\theta}$ (γ)	0.00	0.00
3b	2O(s) → 8Pd(s) + O ₂	3.01 × 10 ²⁶	-0.50	230 - 120 θ
4f	H(s) + O(s) → OH(s) + Pd(s)	2.91 × 10 ¹⁸	1.264	94.6 - 60 θ
4b	OH(s) + Pd(s) → H(s) + O(s)	2.29 × 10 ¹⁹	1.156	120.3 - 30 θ
5f	H(s) + OH(s) → H ₂ O(s) + Pd(s)	6.65 × 10 ¹⁵	1.403	31.80
5b	H ₂ O(s) + Pd(s) → H(s) + OH(s)	2.11 × 10 ¹⁸	1.134	83.3 + 30 θ
6f	2OH(s) → O(s) + H ₂ O(s)	3.89 × 10 ¹⁷	1.244	14.5 + 60 θ
6b	O(s) + H ₂ O(s) → 2OH(s)	1.40 × 10 ¹⁹	1.10	40.7 + 60 θ
7f	H + Pd(s) → H(s)	1.0 (γ)	0.00	0.00
7b	H(s) → H + Pd(s)	1.32 × 10 ¹⁰	1.10	261.7
8f	O + 4Pd(s) → O(s)	1.0 (γ)	0.00	0.00
8b	O(s) → O + 4Pd(s)	1.64 × 10 ¹⁰	1.10	369.7 - 60 θ
9f	OH + 4Pd(s) → OH(s)	1.0 (γ)	0.00	0.00
9b	OH(s) → 4Pd(s) + OH	1.60 × 10 ¹⁰	1.10	227.5 - 30 θ
10f	H ₂ O + 4Pd(s) → H ₂ O(s)	1.0 (γ)	0.00	0.00
10b	H ₂ O(s) → 4Pd(s) + H ₂ O	1.62 × 10 ¹⁰	1.10	43.80

^a For H₂ over a clean, non-CO-poisoned PdO catalyst. The surface site density is $\Gamma = 1.95 \times 10^{-9}$ mol/cm². Site occupancies of O(s), OH(s) and H₂O(s) are 4, based on the experimental observation that each oxygen atom occupies 4 Pd sites [25,45] and have been attested in [25–27,33]. Reaction rates are $k = A \exp(E_a/RT)$ with E_a (kJ/mol). For reactions among surface species, the units of A are mol^{1-m}cm^{2(m-1)}s⁻¹K^{-b}, with m denoting the reaction order based on all surface reactants. For adsorption reactions which are not expressed in terms of a sticking coefficient, the units of A are mol^{1-m-n}cm^{2(m-1)+3n}s⁻¹K^{-b}, with m denoting the reaction order based on all surface reactants and n the reaction order based on all gaseous reactants. γ denotes sticking coefficients and θ the total occupied surface site fraction $\theta = 1 - \theta_{Pd(s)}$. All reactions except R1f and R1b, and site occupancies are taken from [26] without change.

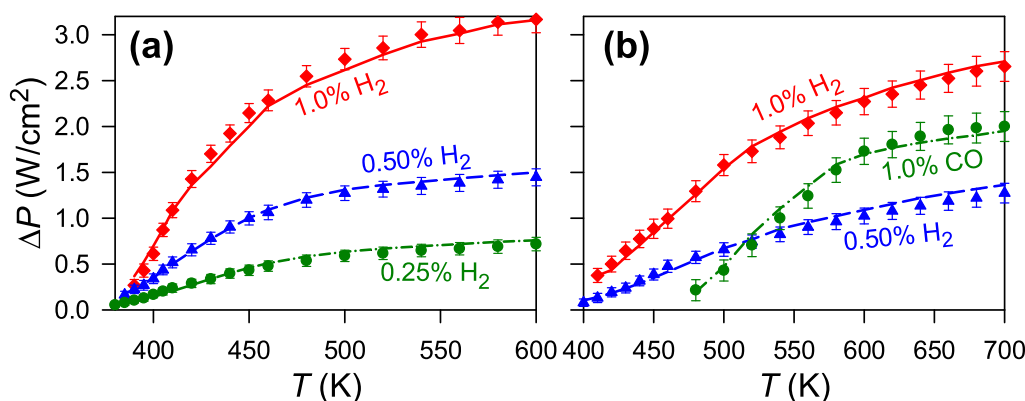


Fig. 5. Measured (symbols) and predicted (lines) heat release rates of: (a) 1.0% (diamonds, solid line), 0.50% (triangles, dashed line) and 0.25% (circles, dashed-dotted line) vol. H₂ in air over a fresh PdO wire (using the reaction mechanism of Table 1) and (b) 1.0% (diamonds, solid line) and 0.50% (triangles, dashed line) vol. H₂, and 1.0% (circles, dashed-dotted line) vol. CO in air over a CO-poisoned PdO wire (using the reaction mechanism of Table 2).

found to be $E_a = 57.33 \pm 0.47$ kJ/mol, $b = 0$ and the pre-exponential factor $A = (2.8 \pm 0.4) \times 10^{26}$ cm⁵mol⁻²s⁻¹ (obtained from the negative slope and extrapolation of the y-intercept of the $\ln(k_{1f})$ versus $1/T$ plot, respectively). Subsequently, desorption of H₂ from the PdO surface ($E_a = 142.82$ kJ/mol and $A = 8.43 \times 10^{22}$ cm²mol⁻¹s⁻¹) was determined from the adsorption rate constants and equilibrium constants of the reversible reaction [26].

Predictions with these fitted rate constants (summarized in Table 1) reproduced excellently the measured heat release rates of 0.25–1.0% vol. H₂ doped in air over the PdO wire, as shown in Fig. 5(a). The exponential sticking coefficient of reaction R3 is taken from [26] without change. Considering that the surface adsorption of oxygen is influenced by both surface temperature and coverage, the sticking coefficient of R3f is modeled as the product of two functions: $\gamma = \gamma_0(T)F(\theta)$. $\gamma_0(T) = e^{-T/540}$ is the sticking coefficient of O₂ on a bare palladium surface, obtained from molecular beam experiment [44], while $F(\theta) = e^{-8.8\theta}$ accounts for the coverage dependency, estimated by a Monte Carlo simulation. It is also worth noting that this model is developed to describe the reaction mechanism on PdO below its decomposition temperature.

4.2. CO-poisoning effect and reaction parameters of individual H₂ and CO on poisoned PdO

Once PdO is exposed to a CO/air or syngas/air mixture, the catalyst experiences a deactivation. Loss of catalytic activity can be classified by type (chemical, thermal and mechanical) and by mechanism (poisoning, fouling, thermal degradation, vapor formation, vapor–solid and solid–solid reactions, and attrition/crushing) as reviewed in Argyle and Bartholomew [46]. While we cannot speculate on the specific mechanism(s) of deactivation, experimental evidence suggests that it is not a chemically induced site blocking but is possibly a catalyst restructuring.

In our experiments, upon exposure to CO or syngas, the catalyst exhibits a loss of activity (attested over a period of many weeks), even when subsequently used only for the oxidation of only H₂. It gradually recovered to a stable level of lower catalytic reactivity when heated in H₂/air or syngas/air flows at temperatures up to 800 K after ~4 h. The poisoning and recovering procedure was repeated using several fresh PdO wires, resulting in a stable and reproducible catalytic reactivity. However, the CO-poisoned

Table 2
Surface reaction mechanism of syngas oxidation over PdO^a.

No.	reaction	A	b	E _a
1f	H ₂ + 2Pd(s) → 2H(s)	1.65 × 10 ²³	0.00	34.65 + α
1b	2H(s) → 2Pd(s) + H ₂	3.66 × 10 ¹⁹	0.992	120.15 + α
2f	CO + Pd(s) → CO(s)	9.89 × 10 ²¹	0.00	117.80 + β
2b	CO(s) → Pd(s) + CO	1.75 × 10 ¹⁶	1.10	241.25 + β
3f	O ₂ + 8Pd(s) → 2O(s)	$e^{-T/540-8.8\theta}$ (γ)	0.00	0.00
3b	2O(s) → 8Pd(s) + O ₂	3.01 × 10 ²⁶	-0.50	230 - 120 θ
4f	H(s) + O(s) → OH(s) + Pd(s)	2.91 × 10 ¹⁸	1.264	94.6 - 60 θ
4b	OH(s) + Pd(s) → H(s) + O(s)	2.29 × 10 ¹⁹	1.156	120.3 - 30 θ
5f	H(s) + OH(s) → H ₂ O(s) + Pd(s)	6.65 × 10 ¹⁵	1.403	31.80
5b	H ₂ O(s) + Pd(s) → H(s) + OH(s)	2.11 × 10 ¹⁸	1.134	83.3 + 30 θ
6f	2OH(s) → O(s) + H ₂ O(s)	3.89 × 10 ¹⁷	1.244	14.5 + 60 θ
6b	O(s) + H ₂ O(s) → 2OH(s)	1.40 × 10 ¹⁹	1.10	40.7 + 60 θ
7f	H + Pd(s) → H(s)	1.0 (γ)	0.00	0.00
7b	H(s) → H + Pd(s)	1.32 × 10 ¹⁰	1.10	261.7
8f	O + 4Pd(s) → O(s)	1.0 (γ)	0.00	0.00
8b	O(s) → O + 4Pd(s)	1.64 × 10 ¹⁰	1.10	369.7 - 60 θ
9f	OH + 4Pd(s) → OH(s)	1.0 (γ)	0.00	0.00
9b	OH(s) → 4Pd(s) + OH	1.60 × 10 ¹⁰	1.10	227.5 - 30 θ
10f	H ₂ O + 4Pd(s) → H ₂ O(s)	1.0 (γ)	0.00	0.00
10b	H ₂ O(s) → 4Pd(s) + H ₂ O	1.62 × 10 ¹⁰	1.10	43.80
11f	CO(s) + 4Pd(s) → C(s) + O(s)	6.39 × 10 ²¹	0.00	174.8 - 47 θ _{CO(s)}
11b	C(s) + O(s) → CO(s) + 4Pd(s)	1.01 × 10 ¹⁹	1.115	62.80
12f	CO(s) + O(s) → CO ₂ (s) + 4Pd(s)	1.41 × 10 ²¹	0.01	42.02
12b	CO ₂ (s) + 4Pd(s) → CO(s) + O(s)	1.00 × 10 ²²	-0.01	150 + 60 θ
13	CO ₂ (s) → CO ₂ + Pd(s)	4.09 × 10 ¹⁴	0.029	65.10

^a For syngas, CO, or H₂ over a CO-poisoned PdO catalyst above light-off temperatures. The surface site density is $\Gamma = 1.95 \times 10^{-9}$ mol/cm². Site occupancies of O(s), OH(s), and H₂O(s) are 4 (see details in the caption of Table 1). Reaction rates are $k = AT^b \exp(E_a/RT)$ with A (units in mol, cm, K and s; see details in the caption of Table 1) and E_a (kJ/mol). γ denotes sticking coefficients. θ is the total occupied surface site fraction $\theta = 1 - \theta_{\text{Pd(s)}}$. R11f is adapted from [50], R12f, R12b and R13 from [22]. All other reactions except R1f, R1b, R2f and R2b, and site occupancies are taken from [26] without change. Correction terms for the activation energies of H₂/CO mixtures are $\alpha = -1.05 \times 10^{-2} \times (2.018 \times 10^{-7} + \theta_{\text{CO(s)}})^{-0.5478} + 14.19$ and $\beta = 5.35 \times 10^{-2} \times (3.952 \times 10^{-7} + \theta_{\text{H(s)}})^{-0.5337} - 22.07$. The expressions for α and β are not valid for pure fuels: α = 0 for H₂-only conditions, while β = 0 for CO-only conditions.

catalyst could only recover to a lower catalytic reactivity compared to the non-CO-poisoned catalyst, and thus the reaction mechanism of Table 1 was not applicable for H₂ oxidation over a CO-poisoned catalyst. Consequently, the CO adsorption/desorption reaction rate constants were assessed by diluting CO in air following a similar procedure as for the H₂ reactions in Section 4.1; the H₂ reaction rate constants were also updated for the poisoned PdO surface. The fitted activation energies for H₂-only and CO-only adsorption reactions on poisoned PdO were 34.65 kJ/mol and 117.80 kJ/mol, respectively. The calculated adsorption entropies ΔS on poisoned PdO were -41.6 J/mol K (400 K) to -37.0 J/mol K (700 K) for H₂, and -209.2 J/mol K (500 K) to -204.9 J/mol K (800 K) for CO. These values were comparable to literature values (on various surfaces) [47–49]. The updated reaction scheme for individual CO and H₂ or H₂/CO mixtures over a CO-poisoned PdO surface is summarized in Table 2. The measured heat release rates on the CO-poisoned catalyst wire with 1.0% H₂, 0.5% H₂ and 1.0% CO and the corresponding predictions with the mechanism in Table 2 were in good agreement with each other as shown in Fig. 5(b). When considering the coverage-dependent activation energies, the reaction mechanisms in Tables 1 and 2 are enthalpically consistent within 4.8% (when the total coverage θ varies from 0 to 1), similar to the previous methane mechanisms on PdO [25–27]. We note in passing that a mechanistic interpretation of the CO-poisoning effect and the potential transitory recovery following an appropriate treatment of the poisoned catalyst goes beyond the scope of this paper and is thus not elaborated here.

Predicted surface coverage of 1% H₂ in air over a clean PdO wire and a CO-poisoned PdO wire, which were calculated using the 2D Fluent code and the detailed reaction mechanisms in Tables 1 and 2, respectively, are shown in Fig. 6 for the temperature range 400–700 K. O(s), OH(s) and free sites Pd(s) had similar magnitudes in both cases, while H(s) and H₂O(s) on the CO-poisoned PdO wire were significantly lower than those on the clean wire.

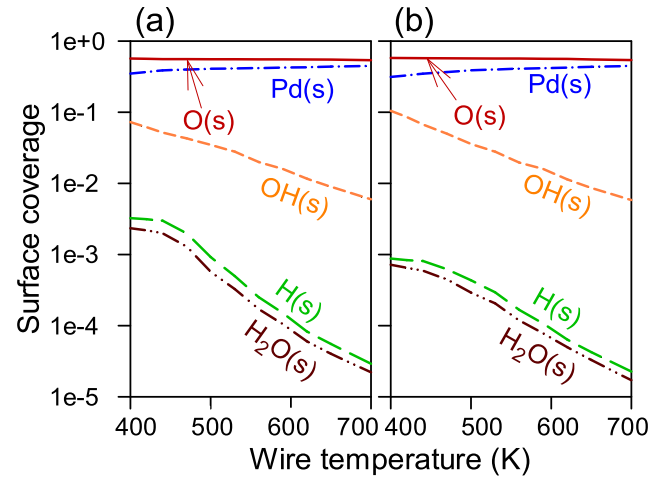


Fig. 6. Computed surface coverage as functions of wire temperature for 1% H₂ in air over (a) a clean PdO wire using the reaction mechanism in Table 1 and (b) a CO-poisoned PdO wire using the reaction mechanism in Table 2.

4.3. Combustion of H₂/CO mixtures and H₂-CO interactions over PdO

We next investigate the reaction of H₂/CO blends over PdO wires and the interactions between the two fuel components. Figure 7(a) compares the measured and predicted heat release rates of H₂ on the catalyst wire using 1.0% vol. H₂ doped in air in the presence of 1.0% CO, 0.5% CO and without CO, while Fig. 7(b) shows the heat release rates due to 1.0% CO accompanied by 0–1.0% H₂ addition. The heat release rates from the two fuel components were distinguished via micro gas chromatograph measurements (micro-GC, type Inficon 3000 with 5% uncertainty for all

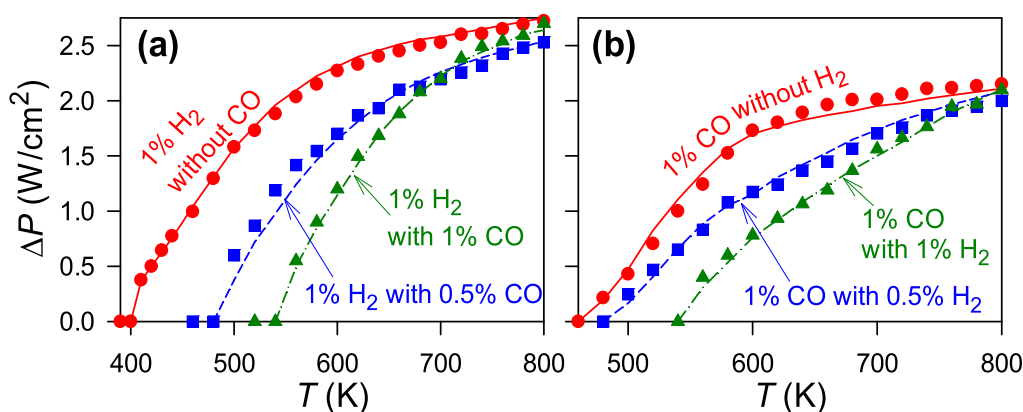


Fig. 7. (a) Heat release rates of 1.0% vol. H_2 in the presence of 0% (circles and solid line), 0.5% (squares and dashed line) and 1.0% (triangles and dotted-dashed line) CO. Heat release rates of the accompanying CO are not plotted as they are irrelevant for the comparisons. (b) Heat release rates of 1.0% vol. CO in the presence of 0%, 0.5% and 1.0% H_2 , notation as in (a). Symbols are measurements and lines are predictions using the catalytic reaction mechanism in Table 2.

gaseous species, with details described elsewhere [51]) that determined the H_2 and CO conversions. It was evident that the added CO and H_2 inhibited each other's catalytic ignition and suppressed their heat release rate. Characteristically, in the presence of 0%, 0.5% and 1.0% CO, H_2 was ignited on the catalyst wire at 410 K, 500 K and 560 K, respectively. In addition, H_2 heat release rates decreased monotonically with increasing CO content at temperatures below ~ 700 K, at which the heat release rate of H_2 in the presence of 1.0% CO exceeded that with 0.5% CO, indicating an inhibition-to-promotion transition of the CO impact on H_2 . Furthermore, the exothermicity of H_2 with 1.0% CO seemed to reach that of H_2 without CO at a temperature slightly higher than 800 K. Figure 7(b) shows similar behaviors for the CO heat release rates with different amounts of H_2 addition, with an observed higher crossover temperature at ~ 780 K.

Based on the above observations, the H_2 -CO inhibiting/promoting effects were incorporated into the detailed catalytic reaction mechanism in Table 2. Additional terms on the activation energies of H_2 /CO adsorption reactions were fitted against the experimental data as power functions of $CO(s)/H(s)$ surface coverage (see α and β in Reactions 1f and 2f of Table 2), which reproduced well the measurements as shown in Fig. 7. The mechanism is not valid for diminishing compositions of one fuel component, as the lowest volumetric content of either fuel component was 0.25%. The interaction parameters α and β have been fine-tuned to reproduce the measurements. Their functional form is such that α and β are monotonically decreasing and monotonically increasing functions of $\theta_{CO(s)}$ and $\theta_{H(s)}$, respectively, and furthermore both α and β are bounded as $\theta \rightarrow 0$. The constants 2.018×10^{-7} and 3.952×10^{-7} within the brackets guarantee bounded values of α and β (otherwise $\alpha \rightarrow \infty$ as $\theta_{CO(s)} \rightarrow 0$ and $\beta \rightarrow \infty$ as $\theta_{H(s)} \rightarrow 0$). The $CO(s)/H(s)$ coverage-dependent correction terms α and β in Reactions 1f and 2f were also added to the desorption reactions to maintain enthalpic balance of the mechanism, although after ignition the desorption reactions were ~ 10 orders of magnitude smaller than the adsorption reactions as discussed in Section 4.1. It is seen that the wide temperature range of the strong CO (H_2) inhibiting effect on H_2 (CO) oxidation over PdO is substantially different from previous studies on other noble metal catalysts, which were carried out in a rectangular flow reactor; these works reported transition temperatures for CO-inhibition on H_2 over much narrower windows of ~ 520 – 550 K on Pt and ~ 500 – 590 K on Rh for $H_2/CO/O_2/N_2$ mixtures with overall equivalence ratios 0.13 and $H_2:CO$ volumetric ratios 1:5–3:1 [43,52].

To decouple the transport effects and to quantify the inhibition-to-promotion transition temperatures at various conditions, addi-

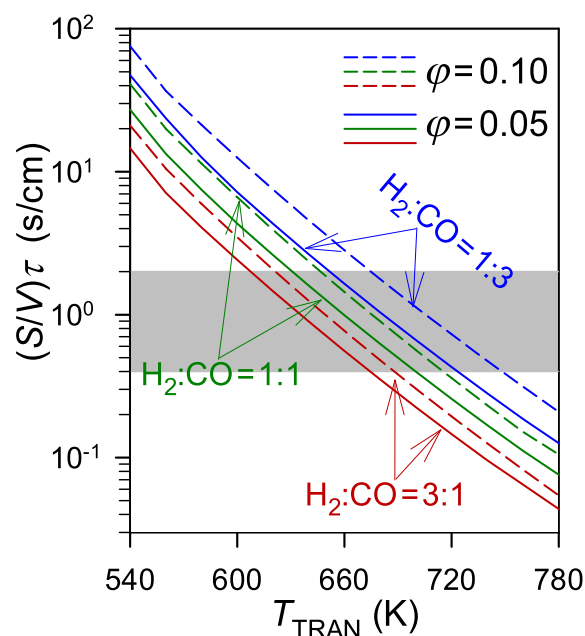


Fig. 8. Inhibition-to-promotion transition temperatures T_{TRAN} versus the product of surface-to-volume ratio S/V and residence time τ , for inlet global equivalence ratios 0.05 (solid lines) and 0.10 (dashed lines), $H_2:CO$ vol. ratios 3:1, 1:1 and 1:3. Shaded area illustrates typical $(S/V)\tau$ in practical power generation systems.

tional simulations were performed using an SPSR with the mechanism in Table 2. The gaseous species governing equations for an SPSR in the absence of gas-phase chemistry are $\rho(Y_{k,IN} - Y_{k,OUT}) = (S/V)\tau \dot{s}_k$, where \dot{s}_k is the catalytic mass reaction rate of the k -th gaseous species, ρ the gas mixture density, Y_k the species mass fraction, S/V the reactor surface-to-volume ratio and τ the residence time. Hence, the transition temperature T_{TRAN} depends on the inlet mixture composition and the product $(S/V)\tau$. T_{TRAN} of H_2/CO /air mixtures with two overall fuel-to-oxygen equivalence ratios (0.05 and 0.10 based on both fuels) and three $H_2:CO$ ratios (3:1, 1:1 and 1:3) are shown in Fig. 8. An artificial gas-phase species CO^* , which had the same transport and thermodynamic properties as CO but was chemically inert, was used in the simulations to facilitate comparisons of the CO inhibiting/promoting chemical effects on H_2 . For a given $(S/V)\tau$, T_{TRAN} was determined as the lowest temperature where H_2 conversion of an H_2/CO mixture exceeded that of the corresponding H_2/CO^* mixture. T_{TRAN}

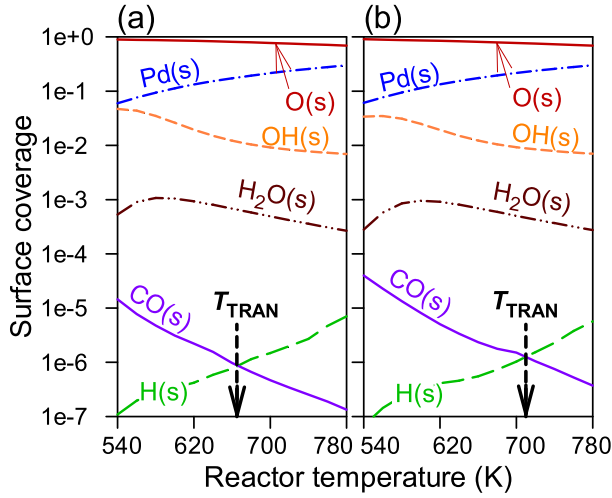


Fig. 9. Computed SPSR surface coverage as functions of reactor temperature for (a) $\phi = 0.05$, $H_2:CO = 1:1$ and (b) $\phi = 0.10$, $H_2:CO = 1:3$. Thick vertical arrows denote transition temperatures for CO impact on H_2 conversion.

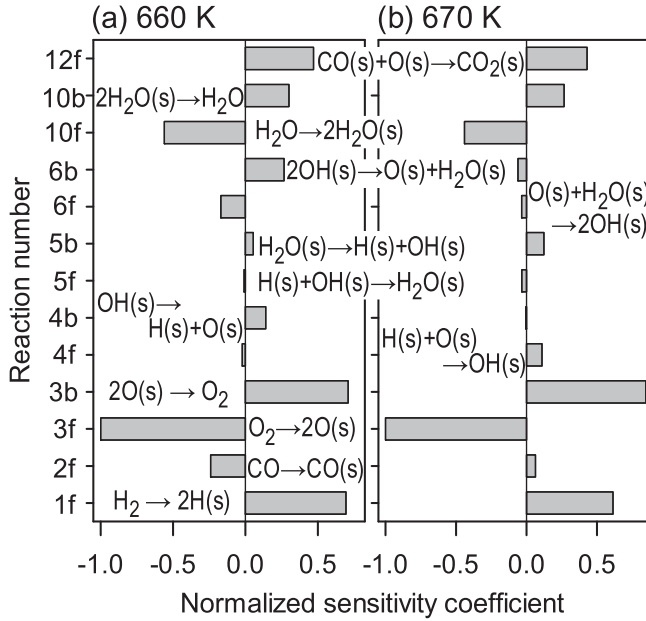


Fig. 10. Sensitivity analysis on H_2 conversion in an SPSR at (a) 660 K (below T_{TRAN}) and (b) 670 K (above T_{TRAN}). $H_2/CO/air$ mixture $\phi = 0.05$ and $H_2:CO = 1:1$, $(S/V)\tau = 1.0$ s/cm.

increased with decreasing $(S/V)\tau$, while for a fixed $(S/V)\tau$, T_{TRAN} increased with rising equivalence ratio and dropping $H_2:CO$ ratio. The shaded area denotes typical $(S/V)\tau$ in practical power generation combustors (~ 0.4 – 2.0 s/cm).

Compared to platinum and rhodium catalysts [43,52], the transition temperatures on PdO occurred at significantly higher surface temperatures and spanned a much broader temperature range for different inlet mixture compositions and equivalence ratios. Characteristically, T_{TRAN} over PdO at $\phi = 0.10$ in the shaded area traversed the temperature range of ~ 620 – 750 K, whereas T_{TRAN} over Pt and Rh and at similar conditions ($\phi = 0.13$) was restricted to a much narrower and lower temperature range of ~ 520 – 560 K. Moreover, contrary to Pt where T_{TRAN} was weakly dependent on the $H_2:CO$ ratio and strongly on the equivalence ratio, T_{TRAN} on PdO was equally dependent on the $H_2:CO$ and ϕ ratios. In power generation gas-turbine systems utilizing the CST methodology [11],

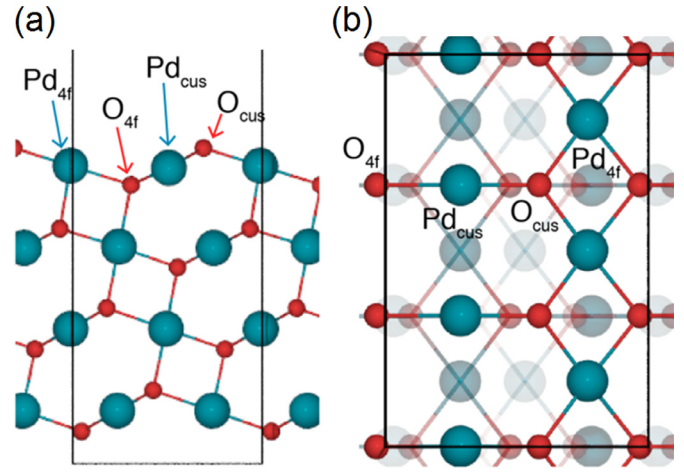


Fig. 11. (a) Side view and (b) top view of the slab model for PdO(101) surface. Cyan and red atoms stand for Pd and O, respectively. As highlighted, there are coordinatively unsaturated (cus) and fourfold-coordinated (4f) saturated Pd and O atoms. (For interpretation of the references to color in this figure legend, the reader is referred to the web version of this article.)

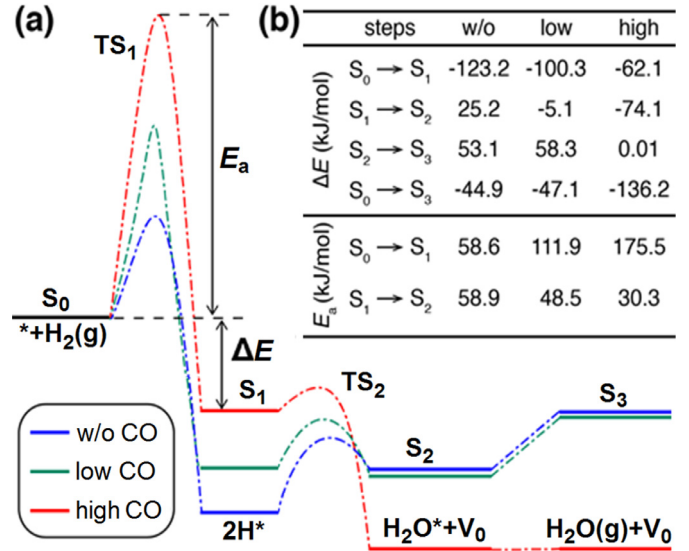


Fig. 12. (a) H_2 combustion energetics without CO presence (blue), with low surface CO coverage (green), and with high surface CO coverage (red). $S_0 \rightarrow S_1$, $S_1 \rightarrow S_2$ and $S_2 \rightarrow S_3$ stand for dissociative adsorption of H_2 onto the PdO(101) surface (i.e. the formation of OH^* groups), water formation and water desorption, respectively. TS_1 and TS_2 are transition states of $S_0 \rightarrow S_1$ and $S_1 \rightarrow S_2$. (b) Tabulated activation energies and reaction enthalpies for the elementary steps. (For interpretation of the references to color in this figure legend, the reader is referred to the web version of this article.)

compressor discharge temperatures span the range 550–750 K depending on the load. Catalytic ignition of syngas mixtures in CST approaches is warranted only for combustor inlet temperatures $T_{IN} > T_{TRAN}$, a condition which (for the investigated stoichiometries in Fig. 8) is typically satisfied for high- H_2 content syngas mixtures.

Figure 9 provides computed surface coverage of two $H_2/CO/air$ blends in an SPSR with $(S/V)\tau = 1.0$ s/cm, as a function of the reactor temperature. As shown in Fig. 8, the transition temperature was 665 K for the mixture with global equivalence ratio 0.05 and $H_2:CO$ ratio 1:1; on the other hand, $T_{TRAN} = 708$ K for $\phi = 0.10$ and $H_2:CO = 1:3$. It is evident that the inhibition-to-promotion transition of CO on H_2 conversion occurred at temperatures where the $H(s)$ surface coverage surpassed $CO(s)$ (see the vertical arrows in Fig. 9). Moreover, the surface species coverage revealed

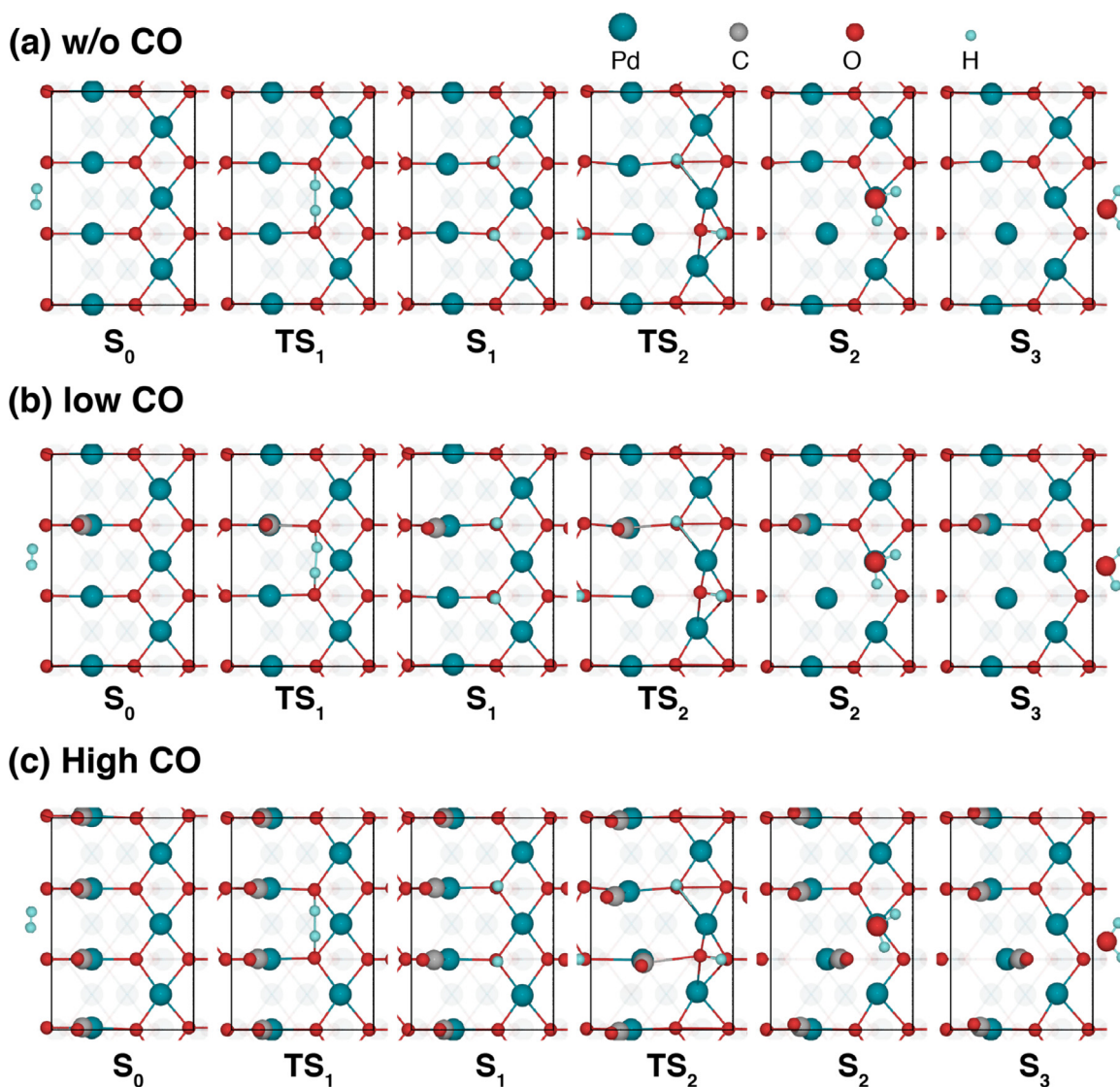


Fig. 13. Top views of configurations along the H_2 oxidation reaction pathways on PdO(101) surfaces (a) without surface CO adsorption, (b) with low surface CO coverage and (c) with high surface CO coverage. Pd, C, O, and H atoms are shown in cyan, gray, red, and light cyan balls, respectively. Reaction step notation as in Fig. 12. Subsurface atoms are shaded for a better clarity. (For interpretation of the references to color in this figure legend, the reader is referred to the web version of this article.)

important differences and similarities between PdO and Pt/Rh catalysts. Contrary to Pt and similar to Rh, O(s) was the dominant species on the PdO surface, hence hindering H_2 and CO adsorptions. The O(s) blocking on the PdO surfaces was also observed in a previous CH_4 study [32]. As shown in Fig. 9, the O(s) dominance was progressively reduced via H_2 and CO reaction routes and more free sites Pd(s) were released with increasing temperature, such that H_2 and CO adsorptions could be initiated. With the reach of a certain temperature (T_{TRAN}), this mechanism overwhelms the H_2 -CO inhibition effect and, consequently, the overall inhibiting effect evolves to be promoting. These observations further reinforce the view of using high H_2 content syngas fuels at full-load high-temperature operating conditions in large turbines with PdO as catalyst in syngas CST combustors. On the other hand, Pt catalysts are more suited to low H_2 :CO ratio fuels and low temperature operations such as recuperative microreactors and part-load or idling operations of large turbines [52].

The normalized sensitivity coefficients of H_2 conversion in an H_2 /CO/air blend with $\varphi = 0.05$ and H_2 :CO = 1:1 are given in Fig. 10, for two surface temperatures of 660 K and 670 K, which are, respectively, below and above T_{TRAN} (665 K). The most important re-

actions are O_2 adsorption/desorption, H_2 adsorption, H_2O desorption and CO_2 production. Reaction 2f (adsorption of CO) changed sign from being negative at 660 K to positive at 670 K, manifesting a shift of the CO kinetic impact on H_2 from inhibitive to promoting.

To further delineate the underlying the H_2 -CO inhibiting effect, DFT simulations were performed to illustrate the oxidation energetics on the PdO(101) surface, which has been theoretically and experimentally confirmed to be the most stable and active PdO surface [53,54]. PdO(101) was modeled with a 4-atomic layer slab of the (101) surface and a (1×3) periodicity. The Brillouin zone was sampled with a $(5 \times 3 \times 1)$ Monkhorst-Pack k -point grid [55]. The PdO(101) surface has two non-equivalent Pd atoms (Pd_{cus} and Pd_{4f}) and O atoms (O_{cus} and O_{4f}), as shown in Fig. 11. It was found via the DFT simulation that, in addition to the competition between H_2 and CO for free surface sites, there exists a direct repelling mechanism between the co-adsorbed H(s) and CO(s).

Figure 12(a) compares the H_2 oxidation energetics on the PdO(101) surface with different levels of surface CO coverage, and the corresponding top views of the H_2 oxidation reaction pathways on PdO(101) are shown in Fig. 13. In the absence of CO, dissociative

adsorption of H_2 has an activation barrier of 58.6 kJ/mol, while two dissociated H atoms bind on top of two neighboring O_{cus} atoms with an adsorption energy of –123.2 kJ/mol. CO molecules preferentially adsorb on top of the Pd_{cus} sites with a relatively stronger adsorption energy of –146.9 kJ/mol. As shown in Fig. 13, the dissociated H atoms turn two surface lattice O atoms to two OH groups. Recombination of these two OH groups leads to the formation of an H_2O molecule and a surface O vacancy with an activation energy of 58.9 kJ/mol. Desorption of H_2O and recovery of O vacancies are relatively fast steps due to the entropy contribution and the overdosed O environment. It is worth noting that the DFT-calculated activation barrier of the rate-determining step of H_2 (58.6 kJ/mol) is in good agreement with the fine-tuned activation energy of 57.33 kJ/mol in Section 4.1 and Table 1.

As summarized in Fig. 12(b), the H_2 adsorption becomes less exothermic with increasing surface CO coverage, accompanied by a significant increase in the dissociation barrier. On the other hand, the water formation step is slightly promoted. Such an inhibition in reaction kinetics is also well supported by the experimentally observed delay in the H_2 ignition temperature in the presence of CO. Another interesting finding concerns the high surface CO coverage case. Although H_2 dissociation has a large barrier E_a to overcome, the overall reaction enthalpy $\Delta E (S_0 \rightarrow S_3)$ is about 90 kJ/mol more exothermic. As shown in Fig. 13(c), with a high surface CO coverage, the formation of surface O vacancy from two OH groups substantially releases the repulsive interactions with co-adsorbed CO molecules, leading to the observed exceptional extra heat release rates.

5. Conclusions

Using fine-tuned wire microcalorimetry experiments and simulations, global and elementary reaction parameters were derived for the oxidation of separate H_2 and CO fuels as well as H_2 –CO fuel blends over PdO catalysts, leading to a detailed catalytic reaction mechanism for syngas oxidation on PdO. The PdO surface was partially deactivated due to CO-poisoning, resulting in reduced H_2 catalytic reactivity. The kinetic coupling of H_2 and CO oxidation developed from an inhibiting two-sided effect due to their competition for surface adsorption and the direct repulsion between co-adsorbed H(s) and CO(s), to a promoting effect caused by alleviated O(s) surface blocking at higher temperatures. The H_2 –CO interactions were explicitly expressed as additional H(s)/CO(s) coverage-dependent terms in the activation energy of the CO/ H_2 adsorption and desorption reactions. With the fitted coverage-dependent activation energies, the developed detailed reaction mechanism captured well the measured H_2 –CO inhibiting/promoting effects, and was further used to quantify the inhibition-to-promotion transition temperatures. The results indicated the advantage of using high H_2 -content syngas fuels at full-load high-temperature operations in palladium-based CST turbine combustors, and set the stage for the further design and optimization of catalytic combustion systems.

Declaration of Competing Interest

The authors declare that they have no known competing financial interests or personal relationships that could have appeared to influence the work reported in this paper.

Acknowledgments

The authors acknowledge the assistance in micro-GC measurements from Prof. Yiguang Ju's group at Princeton University. RS is supported by the Swiss National Science Foundation EPM fellowship (Award Number 178619). LZ acknowledges the use of the

computer time allocation at Extreme Science and Engineering Discovery Environment (XSEDE) supported through the US National Science Foundation (Award Number CHE160084).

References

- [1] J. Mantzaras, Catalytic combustion of syngas, *Combust. Sci. Technol.* 180 (2008) 1137–1168.
- [2] S. Blakey, L. Rye, C.W. Wilson, Aviation gas turbine alternative fuels: a review, *Proc. Combust. Inst.* 33 (2011) 2863–2885.
- [3] C.K. Law, Fuel options for next-generation chemical propulsion, *AIAA J.* 50 (2012) 19–36.
- [4] E.S. Rubin, H. Mantripragada, A. Marks, P. Versteeg, J. Kitchin, The outlook for improved carbon capture technology, *Prog. Energy Combust. Sci.* 38 (2012) 630–671.
- [5] L. Tock, F. Marechal, H_2 processes with CO_2 mitigation: thermo-economic modeling and process integration, *Int. J. Hydrogen Energy* 37 (2012) 11785–11795.
- [6] L.O. Nord, R. Anantharaman, O. Bolland, Design and off-design analyses of a pre-combustion CO_2 capture process in a natural gas combined cycle power plant, *Int. J. Greenh. Gas Control* 3 (2009) 385–392.
- [7] A. Schneider, J. Mantzaras, R. Bombach, S. Schenker, N. Tylli, P. Jansohn, Laser induced fluorescence of formaldehyde and Raman measurements of major species during partial catalytic oxidation of methane with large H_2O and CO_2 dilution at pressures up to 10 bar, *Proc. Combust. Inst.* 31 (2007) 1973–1981.
- [8] A.L. Boehman, O. Corre, Combustion of syngas in internal combustion engines, *Combust. Sci. Technol.* 180 (2008) 1193–1206.
- [9] R. Sui, E. Es-sebbar, J. Mantzaras, N.I. Prasianakis, Experimental and numerical investigation of fuel-lean H_2/CO /air and H_2/CH_4 /air catalytic microreactors, *Combust. Sci. Technol.* 190 (2018) 336–362.
- [10] W.C. Pfefferle, L.D. Pfefferle, Catalytically stabilized combustion, *Prog. Energy Combust. Sci.* 12 (1986) 25–41.
- [11] R. Carroni, T. Griffin, J. Mantzaras, M. Reinke, High-pressure experiments and modeling of methane/air catalytic combustion for power generation applications, *Catal. Today* 83 (2003) 157–170.
- [12] R. Sui, N.I. Prasianakis, J. Mantzaras, N. Mallya, J. Theile, D. Lagrange, M. Friess, An experimental and numerical investigation of the combustion and heat transfer characteristics of hydrogen-fueled catalytic microreactors, *Chem. Eng. Sci.* 141 (2016) 214–230.
- [13] J. Mantzaras, Progress in non-intrusive laser-based measurements of gas-phase thermoscalars and supporting modeling near catalytic interfaces, *Prog. Energy Combust. Sci.* 70 (2019) 169–211.
- [14] P. Forzatti, Status and perspectives of catalytic combustion for gas turbines, *Catal. Today* 83 (2003) 3–18.
- [15] M. Carnello, J.D. Jaén, J.H. Garrido, K. Bakhtmutsky, T. Montini, J.C. Gámez, R.J. Gorte, P. Fornasiero, Exceptional activity for methane combustion over modular Pd/CeO_2 subunits on functionalized Al_2O_3 , *Science* 337 (2012) 713–717.
- [16] D. Ciuparu, M.R. Lyubovsky, E. Altman, L.D. Pfefferle, A. Datye, Catalytic combustion of methane over palladium-based catalysts, *Catal. Rev.* 44 (2002) 593–649.
- [17] D. Ciuparu, L.D. Pfefferle, Support and water effects on palladium based methane combustion catalysts, *Appl. Catal. A – Gen.* 209 (2001) 415–428.
- [18] R. Sui, J. Mantzaras, E. Es-sebbar, R. Bombach, Hetero-/homogeneous combustion of fuel-lean $CH_4/O_2/N_2$ mixtures over PdO at elevated pressures, *Proc. Combust. Inst.* 37 (2019) 5465–5472.
- [19] C.-R. Florén, M. Van den Bossche, D. Creaser, H. Grönbeck, R.-A. Carlsson, H. Korpi, M. Skoglundh, Modelling complete methane oxidation over palladium oxide in a porous catalyst using first-principles surface kinetics, *Catal. Sci. Technol.* 8 (2018) 508–520.
- [20] M. Reinke, J. Mantzaras, R. Schaeren, R. Bombach, A. Inauen, S. Schenker, High-pressure catalytic combustion of methane over platinum: in situ experiments and detailed numerical predictions, *Combust. Flame* 136 (2004) 217–240.
- [21] R. Sui, J. Mantzaras, R. Bombach, A. Denisov, Hetero-/homogeneous combustion of fuel-lean methane/oxygen/nitrogen mixtures over rhodium at pressures up to 12 bar, *Proc. Combust. Inst.* 36 (2017) 4321–4328.
- [22] H. Stotz, L. Maier, A. Boubnov, A.T. Gremminger, J.D. Grunwaldt, O. Deutschmann, Surface reaction kinetics of methane oxidation over PdO, *J. Catal.* 370 (2019) 152–175.
- [23] O. Deutschmann, R. Schmidt, F. Behrendt, J. Warnatz, Numerical modeling of catalytic ignition, *Symp. (Int.) Combust.* 26 (1996) 1747–1754.
- [24] R.W. Sidwell, H. Zhu, R.J. Kee, D.T. Wickham, C. Schell, G.S. Jackson, Catalytic combustion of premixed methane-air on a palladium-substituted hexaluminate stagnation surface, *Proc. Combust. Inst.* 29 (2002) 1013–1020.
- [25] T. Shimizu, H. Wang, Temperature-dependent gas-surface chemical kinetic model for methane ignition catalyzed by in situ generated palladium nanoparticles, *Proc. Combust. Inst.* 33 (2011) 1859–1866.
- [26] Y.X. Xin, S. Lieb, H. Wang, C.K. Law, Kinetics of catalytic oxidation of methane over palladium oxide by wire microcalorimetry, *J. Phys. Chem. C* 117 (2013) 19499–19507.
- [27] Y.X. Xin, H. Wang, C.K. Law, Kinetics of catalytic oxidation of methane, ethane and propane over palladium oxide, *Combust. Flame* 161 (2014) 1048–1054.
- [28] M.M. Wolf, H.Y. Zhu, W.H. Green, G.S. Jackson, Kinetic model for polycrystalline Pd/PdOx in oxidation/reduction cycles, *Appl. Catal. A – Gen.* 244 (2003) 323–340.

- [29] Y.H. Chin, M. García-Diéguez, E. Iglesia, Dynamics and thermodynamics of Pd–PdO phase transitions: effects of Pd cluster size and kinetic implications for catalytic methane combustion, *J. Phys. Chem. C* 120 (2016) 1446–1460.
- [30] T.C. Zhang, D.L. Zhu, N. Yao, F. Qi, C.K. Law, A wire microcalorimetric study of catalytic ignition of methane–air mixtures over palladium oxide, *Proc. Combust. Inst.* 33 (2011) 1819–1825.
- [31] P. Cho, C.K. Law, Catalytic ignition of fuel/oxygen/nitrogen mixtures over platinum, *Combust. Flame* 66 (1986) 159–170.
- [32] T.C. Zhang, Y.X. Xin, Z.Y. Ren, F. Qi, C.K. Law, Catalytic oxidation of methane over PdO in wire microcalorimetry, *Combust. Flame* 160 (2013) 149–154.
- [33] Y.X. Xin, B. Yang, H. Wang, S.L. Anderson, C.K. Law, Kinetics of catalytic oxidation of ethylene over palladium oxide, *Proc. Combust. Inst.* 35 (2015) 2233–2240.
- [34] J. Li, Z.W. Zhao, A. Kazakov, M. Chaos, F.L. Dryer, J.J. Scire, A comprehensive kinetic mechanism for CO, CH₂O, and CH₃OH combustion, *Int. J. Chem. Kinet.* 39 (2007) 109–136.
- [35] P. Giannozzi, S. Baroni, N. Bonini, M. Calandra, R. Car, C. Cavazzoni, D. Ceresoli, G.L. Chiarotti, M. Cococcioni, I. Dabo, A. Dal Corso, QUANTUM ESPRESSO: a modular and open-source software project for quantum simulations of materials, *J. Phys.: Condens. Matter* 21 (2009) 335502.
- [36] A.H. Larsen, J.J. Mortensen, J. Blomqvist, I.E. Castelli, R. Christensen, M. Dułak, J. Friis, M.N. Groves, B. Hammer, C. Hargus, E.D. Hermes, The atomic simulation environment – a python library for working with atoms, *J. Phys.: Condens. Matter* 29 (2017) 273002.
- [37] J.P. Perdew, K. Burke, M. Ernzerhof, Generalized gradient approximation made simple, *Phys. Rev. Lett.* 77 (1996) 3865–3868.
- [38] G. Henkelman, B.P. Uberuaga, H. Jónsson, A climbing image nudged elastic band method for finding saddle points and minimum energy paths, *J. Chem. Phys.* 113 (2000) 9901–9904.
- [39] G. Henkelman, H. Jónsson, Improved tangent estimate in the nudged elastic band method for finding minimum energy paths and saddle points, *J. Chem. Phys.* 113 (2000) 9978–9985.
- [40] S. Zheng, Y. Yang, H. Zhou, The effect of different Hitran databases on the accuracy of the snb and snbck calculations, *Int. J. Heat Mass Transf.* 129 (2019) 1232–1241.
- [41] H.K. Moffat, R.J. Kee, J.F. Grcar, J.A. Miller, Surface PSR: a Fortran program for modeling well-stirred reactors with gas and surface reactions, Sandia National Laboratories, USA, 1993 Report No. SAND91-8001.
- [42] C. Appel, J. Mantzaras, R. Schaeren, R. Bombach, A. Inauen, B. Kaeppli, B. Hemmerling, A. Stamparoni, An experimental and numerical investigation of homogeneous ignition in catalytically stabilized combustion of hydrogen/air mixtures over platinum, *Combust. Flame* 128 (2002) 340–368.
- [43] R. Sui, J. Mantzaras, R. Bombach, H₂ and CO heterogeneous kinetic coupling during combustion of H₂/CO/O₂/N₂ mixtures over rhodium, *Combust. Flame* 202 (2019) 292–302.
- [44] T. Engel, Molecular-beam investigation of He, CO, and O₂ scattering from Pd(111), *J. Chem. Phys.* 69 (1978) 373–385.
- [45] J.C. Andrae, Å. Johansson, P. Björnbom, A. Rosén, OH desorption energies for a palladium catalyst characterised by kinetic modelling and laser-induced fluorescence, *Surf. Sci.* 563 (2004) 145–158.
- [46] M. Argyle, C. Bartholomew, Heterogeneous catalyst deactivation and regeneration: a review, *Catalysts* 5 (2015) 145–269.
- [47] E. Garrone, B. Bonelli, C.O. Areán, Enthalpy–entropy correlation for hydrogen adsorption on zeolites, *Chem. Phys. Lett.* 456 (2008) 68–70.
- [48] X. Xia, R. Naumann d'Alnoncourt, M. Muhler, Entropy of adsorption of carbon monoxide on energetically heterogeneous surfaces, *J. Therm. Anal. Calorim.* 91 (2008) 167–172.
- [49] J.F. Kramer, S.A.S. Reihani, G.S. Jackson, Low temperature combustion of hydrogen on supported Pd catalysts, *Proc. Combust. Inst.* 29 (2002) 989–996.
- [50] C. Karakaya, L. Maier, O. Deutschmann, Surface reaction kinetics of the oxidation and reforming of CH₄ over Rh/Al₂O₃ catalysts, *Int. J. Chem. Kinet.* 48 (2016) 144–160.
- [51] H. Zhao, L. Wu, C. Patrick, Z. Zhang, Y. Rezgui, X. Yang, G. Wysocki, Y. Ju, Studies of low temperature oxidation of n-pentane with nitric oxide addition in a jet stirred reactor, *Combust. Flame* 197 (2018) 78–87.
- [52] X. Zheng, J. Mantzaras, R. Bombach, Kinetic interactions between hydrogen and carbon monoxide oxidation over platinum, *Combust. Flame* 161 (2014) 332–346.
- [53] J. Rogal, K. Reuter, M. Scheffler, Thermodynamic stability of PdO surfaces, *Phys. Rev. B* 69 (2004) 075421.
- [54] N.M. Martin, M. Van den Bossche, A. Hellman, H. Grönbeck, C. Hakanoglu, J. Gustafson, S. Blomberg, N. Johansson, Z. Liu, S. Axnanda, J.F. Weaver, Intrinsic ligand effect governing the catalytic activity of Pd oxide thin films, *ACS Catal.* 4 (2014) 3330–3334.
- [55] H.J. Monkhorst, J.D. Pack, Special points for brillouin-zone integrations, *Phys. Rev. B* 13 (1976) 5188–5192.